



In situ grown Ni phosphide nanowire array on Ni foam as a high-performance catalyst for hydrazine electrooxidation



He Wen^a, Li-Yong Gan^a, Hong-Bin Dai^{a,*}, Xiao-Ping Wen^a, Lin-Song Wu^a, Hui Wu^b, Ping Wang^{a,*}

^a School of Materials Science and Engineering, Key Laboratory of Advanced Energy Storage Materials of Guangdong Province, South China University of Technology, Guangzhou 510641, PR China

^b NIST Center for Neutron Research, National Institute of Standards and Technology, Gaithersburg, MD, 20899-6102, United States

ARTICLE INFO

Keywords:
Direct hydrazine fuel cell
Hydrazine electrooxidation
Electrocatalyst
Transition metal phosphides

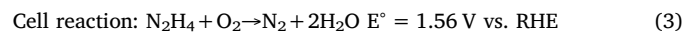
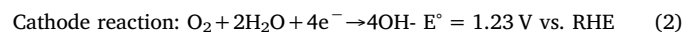
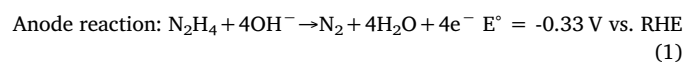
ABSTRACT

Synthesis of high-performance and cost-effective electrocatalysts towards hydrazine electrooxidation is vital to develop the direct hydrazine fuel cell (DHFC) as a viable energy conversion technology. Herein, we report a combined experimental and theoretical study of nickel phosphides (Ni_xP) as promising catalysts for hydrazine electrooxidation. Ni_xP nanowire array supported on a Ni foam (NF) was synthesized by a one-step phosphorization method using hypophosphite as a P-source. $Ni_{12}P_5$ and Ni_2P phases are observed as the products of the direct phosphorization of commercial NF under the applied conditions with Ni_2P nanoparticles exclusively distributing on the surface of $Ni_{12}P_5$. The Ni_xP/NF catalyst exhibits a synergistic capabilities of exceptionally high activity, excellent durability and nearly 100% selectivity towards the complete electrooxidation of hydrazine in alkaline condition, which is among the best performance reported on hydrazine electrooxidation catalysts. First-principles calculations have been conducted to gain insight into the catalytic mechanism of Ni phosphides towards hydrazine electrooxidation.

1. Introduction

Fuel cells are expected to play an important role in the future energy system, as they promise highly efficient and reliable conversion of chemical energy into electric energy, and the latter is feasible for diverse applications, from large stationary power plants to transportation vehicles and to the vast types of portable devices. Depending upon the fuel type, fuel cells can be operated across a broad range of operation temperatures and exhibit remarkably different performance specifications [1,2]. In the quest of viable fuel cells for vehicular or portable applications, direct hydrazine fuel cell (DHFC) using hydrous hydrazine ($N_2H_4\cdot H_2O$) as a fuel has attracted considerable attention owing to its many favorable attributes [3]. Hydrous hydrazine is a carbon-free fuel with high energy density, low material cost and satisfactory stability at ambient conditions. The electrooxidation of hydrazine (N_2H_4) via a 4-electron pathway, as described by Eqs. (1)–(3), yields a theoretical cell voltage of +1.56 V, which is higher than hydrogen-air and most liquid fuel cells [4–6]. DHFC can be operated at near-ambient temperatures and the resulting dinitrogen and water are eco-friendly. Importantly, DHFC does not require the usage of prohibitively expensive noble metals as electrocatalyst, which is a distinct advantage over hydrogen-air and direct alcohol fuel cells [3,7–9]. A major concern that hampers

the practical application of DHFC is the toxicity and mutagenicity of hydrous hydrazine, whereas it can be addressed through the formation of solid hydrazone by reacting hydrous hydrazine with carbonyl-containing polymer according to Tanaka and coworkers [10]. Hydrazone is safe and releases hydrous hydrazine upon contacting with warm water.



Seeking advanced electrocatalysts is paramount in the development of DHFC energy conversion technology. In the past decades, a number of noble and non-noble transition metals and their alloys or compounds had been identified as active catalysts for the electrooxidation of hydrazine [11–25]. In a general view, non-noble metal catalysts exhibited higher activity but lower durability than the noble metal catalysts in alkaline conditions. Electrocatalytic performances of non-noble metal catalysts can be ameliorated through two approaches. One is to enhance the intrinsic activity of electrocatalyst via alloying or formation of metal compounds. The other is to increase the number of active sites, primarily via nanostructuring the electrocatalytic materials. In practice,

* Corresponding authors.

E-mail addresses: mshbdai@scut.edu.cn (H.-B. Dai), mspwang@scut.edu.cn (P. Wang).

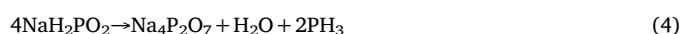
these two approaches are always adopted simultaneously to boost the performance [26]. This is evident from the recent development of nickel phosphide (Ni_xP) catalyst. According to Sun et al., the in situ grown Ni_2P nanoarray on Ni foam ($\text{Ni}_2\text{P}/\text{NF}$) dramatically outperformed the relevant catalysts for hydrazine electrooxidation, thereby representing an encouraging progress in the development of DHFC [27]. However, the relation between the phase structure and the catalytic properties of Ni phosphide remains to be established and the mechanism underlying the remarkable activity enhancement upon phosphidation of Ni is still unclear. Understanding these fundamental issues is clearly crucial for successful future searches and development of high-performance catalysts for hydrazine oxidation.

Herein, we report a systematic study of nickel phosphide (Ni_xP) catalyst towards the electrooxidation of hydrazine. The Ni_xP nanoarray was in situ grown on NF using a straightforward phosphidation method. The as-prepared $\text{Ni}_x\text{P}/\text{NF}$ exhibited extraordinary performance in terms of activity, durability and selectivity towards the complete electrooxidation of hydrazine. First-principles calculations have also been conducted to shed light on the mechanism of such outstanding electrocatalytic performance of Ni phosphides towards hydrazine electrooxidation.

2. Experimental

2.1. Electrocatalyst synthesis

Sodium hypophosphate (NaH_2PO_2 , 99.0%) was purchased from Macklin and used as received. Ni foam (NF, $\geq 99\%$) with a thickness of 1.80 mm, an area density of about 650 g m^{-2} and an average pore size from 0.25 to 0.80 mm was purchased from Incoatm. Prior to phosphorization, the NF was cleaned by ultrasonication in ethanol for 10 min to remove surface impurities. Typically, a piece of cleaned NF ($1 \times 1.45 \text{ cm}^2$) was loaded into a quartz boat and around 2.0 g of NaH_2PO_2 was placed 1 cm away from the NF at the upstream side. The boat was heated up to 300°C at a ramping rate of 2°C min^{-1} and then held at this temperature for 3.0 h under a flowing Ar atmosphere. After being naturally cooled down to room temperature, the obtained NF sample was washed with deionized water and ethanol, and then dried in vacuum. The chemical reactions in the phosphorization process can be illustrated by Eqs. (4) and (5).



For comparison, Ni_xP film was also grown on NF using an electroplating method. The plating solution contained 0.3 M NaH_2PO_2 , 0.1 M $\text{NiSO}_4 \cdot 6\text{H}_2\text{O}$, 0.1 M NaCl, and 0.15 M H_3BO_3 , with a pH value of 4.7. The electrodeposition was performed at 30°C under a constant potential of -0.85 V vs. saturated calomel electrode for 10 min.

2.2. Electrochemical measurements

Electrochemical measurements were performed in an electrochemical workstation (PARSTAT MC 2000) using a standard three-electrode cell at ambient temperature. The electrochemical cell consists of a catalytic electrode, a Hg/HgO (with 1 M NaOH) and a Pt foil as the working electrode, reference electrode and counter electrode, respectively. Potentials, measured versus Hg/HgO , were referenced to the reversible hydrogen electrode (RHE) by adding a value of $(0.059 \times \text{pH} + 0.098) \text{ V}$. Before each measurement, the electrolyte solution was deoxygenated by bubbling Ar gas for at least 15 min. All measurements of linear sweep voltammetry (LSV) were performed in an alkaline medium (1.0 M NaOH) at a scan rate of 20 mV s^{-1} . The double-layer capacitances (C_{DL}) of the catalyst samples were determined from the scan-rate dependence of capacitive current in cyclic voltammetry (CV) measurements. Electrochemical impedance spectroscopy (EIS)

experiments were performed with above three-electrode cell system while sweeping the frequency from 100 kHz to 100 mHz with a 5 mV amplitude at the onset potential. The curve fitting was performed by Zview software. In determination of Faradic efficiency (FE), the amount of generated gas during anode electrooxidation process was measured by a classic water-displacement method. The FE was calculated by comparing the experimentally measured gas amount with theoretical value.

2.3. Characterization

The morphology and microstructure of the catalyst samples were observed using field-emission scanning electron microscope (FE-SEM, ZEISS MERLIN) and high-resolution transmission electron microscopy (HRTEM, JEOL-2100 F). The phase structure was identified using X-ray diffraction (XRD, Rigaku RINT 2000, Cu K α radiation, $\lambda = 1.5418 \text{ \AA}$). X-ray photoelectron spectroscopy (XPS, Thermo Scientific K-ALPHA+, Al K α X-ray source) technique was used to analyse the chemical states of the constituent elements of the catalyst samples. In the XPS measurements, high-resolution scans of elemental lines were recorded at 50 eV pass energy of the analyzer. All the BEs were calibrated using the C1s peak at 284.8 eV of the adventitious carbon as an internal standard. The curve fitting was performed by XPS PEAK 4.1 software.

2.4. Computational methods

First-principles calculations were performed based on density functional theory implemented in Vienna ab-initio Simulation Package [28]. Spin-polarized generalized gradient approximation of Perdew-Burke-Ernzerhof exchange-correlation functional was used to describe the exchange-correlation interaction [29]. A plane wave cutoff energy of 500 eV was used in all calculations, sufficiently ensuring the convergence [30–32]. The surfaces were modelled by a five-layer (3×3) unit cell for f.c.c. Ni (111) and a six-layer (1×1) unit cell for hexagonal Ni_2P (001). Specifically, Ni_3P_2 -terminated plane was found to be predominantly exposed for Ni_2P (001) surface [33]. The vacuum thickness was set to be at least 20 \AA to eliminate unphysical interaction between the replicas of the slab. In each calculations, the top three layers together with the adsorbates were fully relax in all dimensions till all residual forces have declined below 0.02 eV/\AA . A standard dipole correction was employed due to asymmetric slabs [34]. The Brillouin zone was sampled by Gamma-centered $5 \times 5 \times 1$ and $7 \times 7 \times 1$ k-meshes for the (3×3) Ni (111) and (1×1) Ni_2P (001) supercells, respectively.

The adsorption energy (E_{ads}) of adsorbates on surfaces was defined as

$$E_{\text{ads}} = E_{\text{X/surface}} - E_{\text{X}} - E_{\text{surface}} \quad (6)$$

where $E_{\text{X/surface}}$, E_{X} and E_{surface} are the total energies of X adsorbed surfaces, gas-phase species and clean surfaces, respectively. The Gibbs free energy changes of each elementary step were calculated as

$$\Delta G = \Delta E + \Delta ZPE - T\Delta S \quad (7)$$

where ΔZPE and ΔS are the zero-point energy and entropy differences, respectively. Temperature was set to be 298 K. The entropies and ZPE were calculated based on additional vibrational frequency analysis [35].

3. Results and discussion

3.1. Catalyst characterization

Direct reaction of transition metals with P vapor or gaseous PH_3 at elevated temperatures provides a straightforward approach to produce metal phosphides [27,36–40]. In the present study, we employed this simple method to prepare Ni_xP nanoarray on the NF surface using

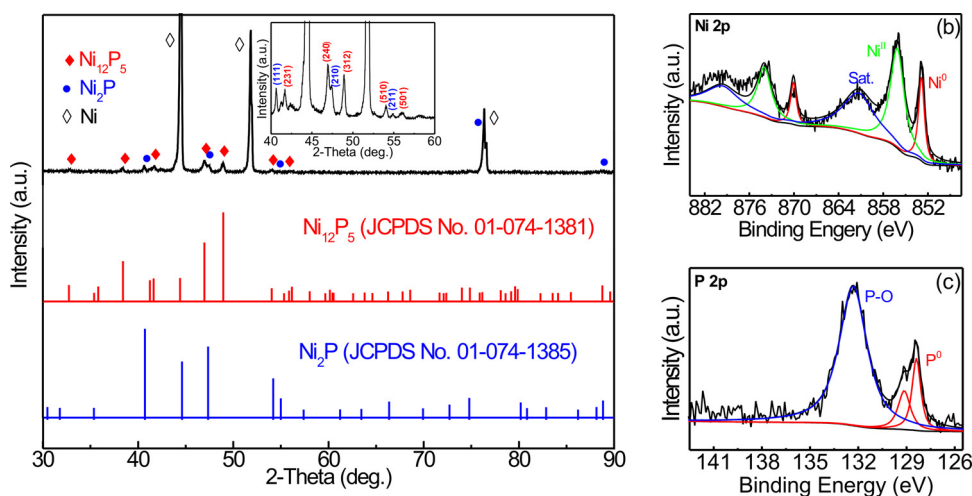


Fig. 1. (a) XRD pattern, (b) Ni 2p XPS spectrum, and (c) P 2p XPS spectrum of the post-phosphidated Ni foam. The inset in (a) showed a magnified view of the region of interest.

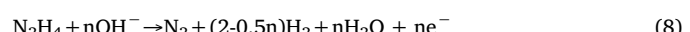
NaH_2PO_2 as a P source. The resulting sample from direct phosphorization of NF was denoted as $\text{Ni}_x\text{P}/\text{NF}$ (DP). It was observed that the NF sample well retained its 3D porous structure after phosphorization, but with a notable colour change from the initial silver grey to black (Fig. S1, Supplementary material). XRD analysis of the post-phosphidated sample evidences the formation of two crystalline nickel phosphide phases with slightly different stoichiometries. As seen in Fig. 1a, besides the strong peaks of the NF substrate, the diffraction peaks at 41.7° , 46.9° , and 48.9° can be well indexed to the tetragonal Ni_{12}P_5 (JCPDS card 01-074-1381) and those at 40.7° , 47.4° , and 54.2° to the hexagonal Ni_2P phase (JCPDS card 01-074-1385). From the weight change before and after phosphidation, the amount of the in situ formed Ni_xP on Ni foam was estimated to be around $15.5 \sim 18.0 \text{ mg cm}^{-2}$. The $\text{Ni}_x\text{P}/\text{NF}$ (DP) sample was further examined by the surface-sensitive XPS technique to determine the chemical states of the constituent elements. As seen in Fig. 1b and c, both Ni and P elements showed two chemically different entities. For Ni, the peak at 856.1 eV can be safely assigned to Ni^{II} species resulted from the possible surface oxidation of the sample upon air exposure. The other $\text{Ni } 2p_{3/2}$ signal at 853 eV exhibited a positive shift of binding energy (BE), $\sim 0.5 \text{ eV}$, compared to the metallic Ni^0 . Meanwhile, the P $2p_{3/2}$ and $2p_{1/2}$ peaks at 129.1 and 128.5 eV showed negative shifts of BE, $\sim 1.4 \text{ eV}$, compared to the pristine P⁰. These results clearly indicate an electron transfer from Ni to P, which is consistent with the observed formation of nickel phosphides.

Morphology observation of the $\text{Ni}_x\text{P}/\text{NF}$ (DP) sample by FE-SEM (Fig. 2a–c) found that the surface of NF was entirely covered by high-density arrays of vertically aligned nanowires. These nanowires showed poorly defined shapes, varied diameters ranging from 200 to 400 nm, and relatively long lengths up to several micrometers. Fig. 2d–g present the two-dimensional elemental mapping results that were acquired in high-angle annular dark-field scanning transmission electron microscopy (HAADF-STEM) mode in combination with energy dispersive X-ray spectroscopy (EDS) analysis. It is evident that Ni and P elements dispersed homogeneously throughout the nanowires. The selected area electron diffraction (SAED) analysis and HRTEM observation further help identify the phase structures as well as their spatial distributions. As seen in Fig. 2i, the SAED pattern clearly showed two sets of diffraction spots separately corresponding to the Ni_{12}P_5 and Ni_2P crystalline phases. In the representative HRTEM images (Fig. 2j, k), the lattice fringes with interplanar spacings of 0.610 and 0.437 nm intersected with an interplanar angle of 69° could be safely assigned to Ni_{12}P_5 , while the lattice fringes with distance of 0.338 and 0.293 nm and an interplanar angle of 90° belong to the Ni_2P phase. The SAED and HRTEM observations are in good agreement with the XRD result.

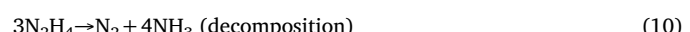
Particularly, the HRTEM results revealed that the Ni_2P phase exclusively distributes on the surface of the Ni_{12}P_5 phase (Fig. 2j and k). Such spacial phase distribution from the outlayer Ni_2P to the internal Ni_{12}P_5 with the decreased P content inwards reflects the diffusion and phosphorization pathway from the outer P source.

3.2. Electrocatalytic performance for N_2H_4 oxidation

The electrocatalytic properties of the $\text{Ni}_x\text{P}/\text{NF}$ (DP) sample towards hydrazine oxidation were examined and compared with those of the neat NF and the $\text{Ni}_x\text{P}/\text{NF}$ (EP) sample prepared using an electroplating method. As shown in Fig. 3a, the CV curves of all three catalyst samples showed an anodic peak in the forward scan, which primarily correspond to hydrazine oxidation. Judging from the peak currents and peak potentials, the directly phosphidated $\text{Ni}_x\text{P}/\text{NF}$ (DP) sample exhibited the highest activity towards hydrazine oxidation, followed by the $\text{Ni}_x\text{P}/\text{NF}$ (EP) and NF samples. The same ascending order of activity was also observed in the LSV measurements (Fig. 3b). In comparison with the neat NF, the $\text{Ni}_x\text{P}/\text{NF}$ (EP) sample showed a reduced onset potential of 57 mV and a one-fold increase of current density, while the $\text{Ni}_x\text{P}/\text{NF}$ (DP) sample obtained from direct phosphidation of NF exhibited further remarkably enhanced catalytic activity. It showed an onset potential of -0.08 V vs. RHE and a current density of 580 mA cm^{-2} at 0.30 V , which is comparable to the top notch hydrazine electrooxidation catalysts reported up to date (Table S1, Supplementary material). The remarkable activity advantage of the $\text{Ni}_x\text{P}/\text{NF}$ (DP) over the NF and $\text{Ni}_x\text{P}/\text{NF}$ (EP) catalysts should be ascribed to the formation of the nanostructured Ni_xP phases with an enhanced intrinsic activity and/or the increased number of active sites, as stated below.



where n is the number of reaction electrons (n = 1, 2, 3, and 4).



In the DHFC, anodic oxidation of hydrazine ideally follows a 4-electron-reaction (Eq. (1)), yielding N_2 and H_2O as the final products. However, practically the electrooxidation of hydrazine may proceed via different reaction pathways, which involve different numbers of electrons transferred, as described by Eq. (8). Furthermore, the electro-oxidation reactions may be entangled by the catalytic decomposition of hydrous hydrazine, as described by Eqs. (9) and (10). All these side-reactions may result in a deteriorated fuel efficiency. In the present study, we observed that the hydrous hydrazine fuel solution was stable

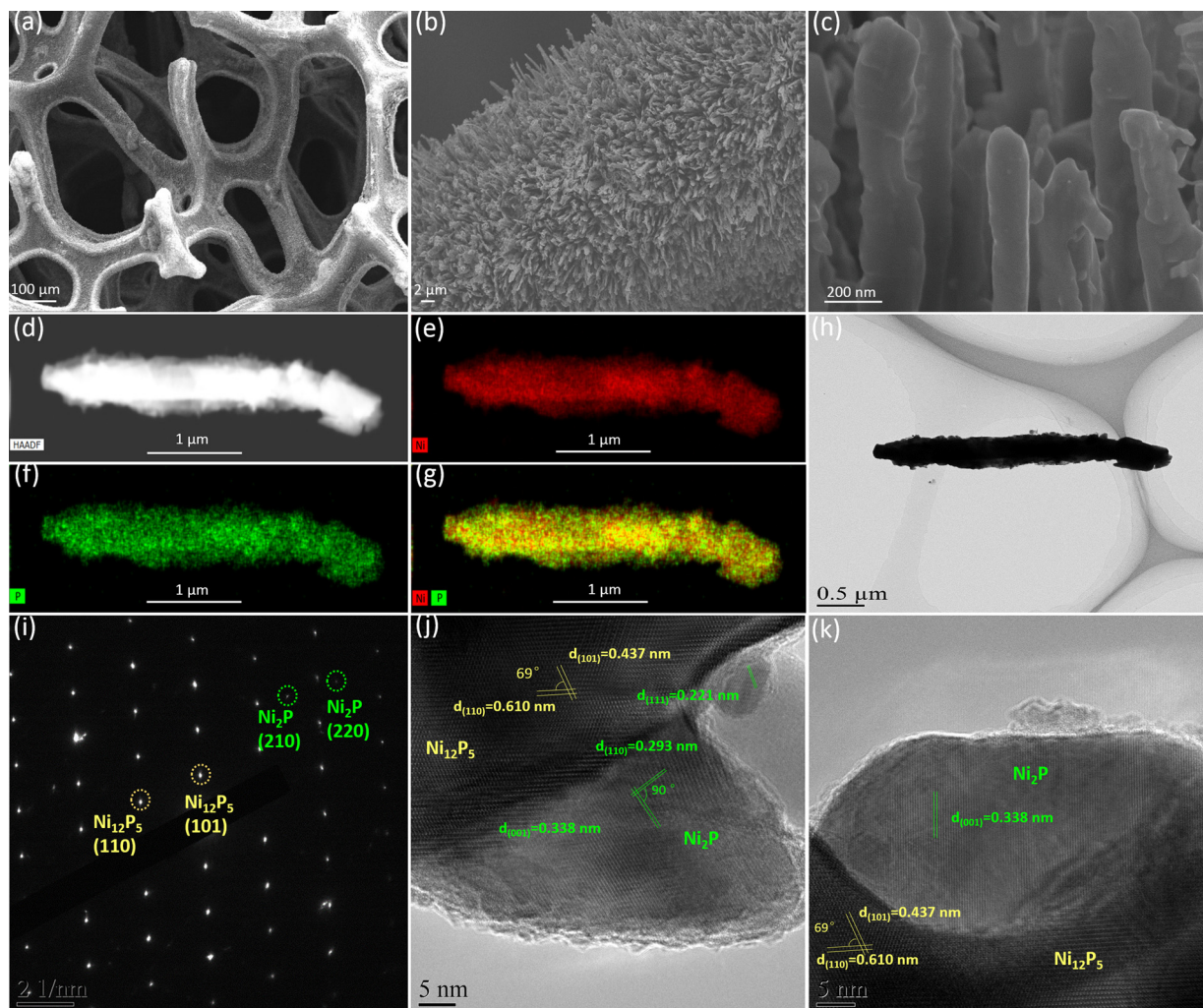


Fig. 2. (a), (b) and (c) FE-SEM images at different resolutions; (d)-(g) HAADF-STEM image and corresponding EDS maps for Ni, P and combined image, respectively. (h) TEM image and (i) the corresponding SAED pattern; (j) and (k) Two representative HRTEM images of $\text{Ni}_x\text{P}/\text{NF}$ (DP) catalyst.

upon contacting with the $\text{Ni}_x\text{P}/\text{NF}$ (DP) catalyst, suggesting that the hydrazine decomposition over the $\text{Ni}_x\text{P}/\text{NF}$ (DP) catalyst should be negligible at open circuit potential. In an effort to determine the number of the transferred electrons during hydrazine oxidation, we measured the current density dependence of the anodic gas generation rates. As shown in Fig. 3c, the measured gas amounts were in excellent agreement with the values calculated from the 4-electron-reaction in the examined current density range, indicating a nearly 100% FE for the electrooxidation of hydrazine over the $\text{Ni}_x\text{P}/\text{NF}$ (DP) catalyst.

In order to gain insight into the variations of electrocatalytic activity, we conducted CV measurements at varied scan-rates to determine the C_{DL} (Fig. S2, Supplementary material) and used EIS technique to measure the charge-transfer resistance (R_{ct}) of a series of catalysts. It was found that the C_{DL} of the $\text{Ni}_x\text{P}/\text{NF}$ (DP) catalyst nearly doubled that of the $\text{Ni}_x\text{P}/\text{NF}$ (EP) and was about 15-fold higher than that of the neat NF (Fig. 3d). Since the electrochemical active surface area (ECSA) is proportional to the C_{DL} , these results clearly indicate that the direct phosphorization of NF provided a simple but effective method for maximizing the active surface area of the electrocatalyst. This was directly evidenced by the morphology observations. As seen in the SEM images, the $\text{Ni}_x\text{P}/\text{NF}$ (EP) sample showed a relatively smooth surface morphology (Fig. S3, Supplementary material), which was in sharp contrast to the formation of nanowire arrays in the $\text{Ni}_x\text{P}/\text{NF}$ (DP) sample (Fig. 2b and c). The EIS measurement results further showed that coating NF with Ni_xP , particularly via direct phosphorization of

NF, caused a notable decrease of R_{ct} (Fig. 3e). This was supported by our first-principles calculations (Fig. S4, Supplementary material). The calculated density of states revealed that both the Ni_{12}P_5 and Ni_2P phases are conductors with continuous energy bands near the Fermi level, thus ensuring efficient electron transfers during N_2H_4 electro-oxidation.

Long-term stability is also an important criterion for evaluating the N_2H_4 electrooxidation catalysts. In the present study, we tested and compared the durabilities of the $\text{Ni}_x\text{P}/\text{NF}$ (DP) and relevant catalysts using chronoamperometry and CV methods. In the chronoamperometry measurements, as shown in Fig. 3f, all three electrocatalysts showed rapidly decreased current densities at the initial reaction stage. After 10,000 s of constant-potential measurement, the $\text{Ni}_x\text{P}/\text{NF}$ (DP) catalyst still retained 80.5% of its initial activity. In sharp contrast, the NF and $\text{Ni}_x\text{P}/\text{NF}$ (EP) samples showed only 34.8% and 63.5% of their initial levels, respectively. To gain insight into the improved stability, we conducted XPS analyses of the as-prepared and the post-used catalyst samples (Fig. S5, Supplementary material). It was observed that the chemical state of Ni species in the $\text{Ni}_x\text{P}/\text{NF}$ (DP) sample showed no significant change, whereas the Ni^{II} signal became remarkably strengthened in the $\text{Ni}_x\text{P}/\text{NF}$ (EP) and NF samples after the stability test. These results suggested the excellent stability of $\text{Ni}_x\text{P}/\text{NF}$ (DP) catalyst towards hydrazine electrooxidation might stem from the alleviated surface oxidation of Ni_xP coating. In the CV measurements, the anodic current at 0.2 V vs. RHE was periodically extracted and plotted

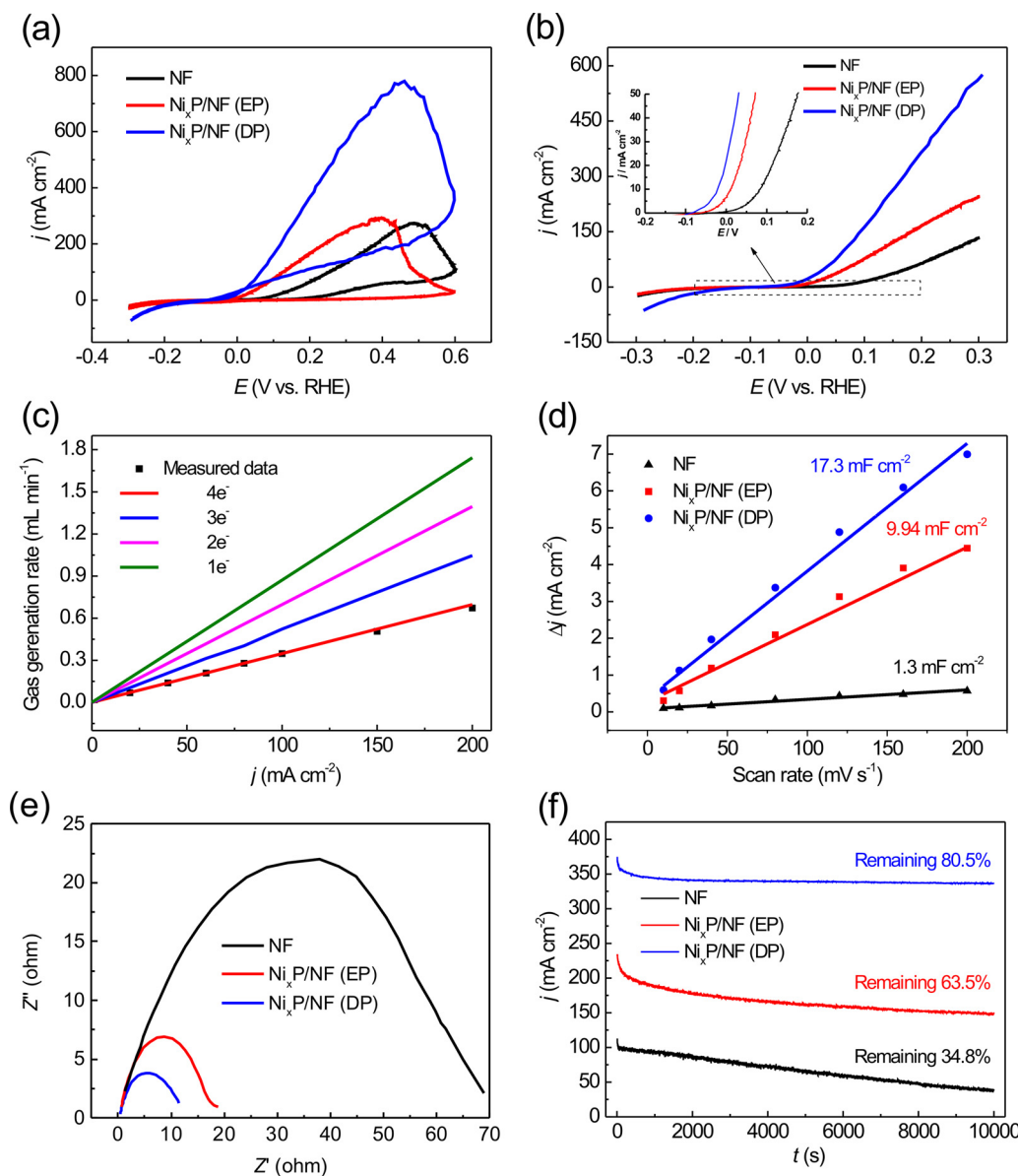


Fig. 3. (a) CV curves and (b) LSV profiles at 30 °C in a solution containing 0.1 M $\text{N}_2\text{H}_4\text{H}_2\text{O}$ and 1.0 M NaOH at a scan rate of 20 mV s $^{-1}$. The inset shows a zoomed-in view of the onset potential region of the examined electrocatalysts; (c) The current density dependence of the anodic gas generation rates; (d) The capacitive current densities at open circuit potential as a function of scan rate; (e) EIS Nyquist plots at onset potentials; (f) Chronoamperometric curves of the examined electrocatalysts at a constant-potential of 0.2 V in a solution containing 3.0 M $\text{N}_2\text{H}_4\text{H}_2\text{O}$ and 1.0 M NaOH.

against the cycle number (Fig. S6, Supplementary material). The $\text{Ni}_x\text{P}/\text{NF}$ (DP) catalyst exhibited an activity loss of only 14% after 1000 CV cycles, which is much lower than those of the $\text{Ni}_x\text{P}/\text{NF}$ (EP) (48.7%) and NF (51.4%). SEM observations found that the morphological feature of the catalyst was well maintained after long-term operation (Fig. S7, Supplementary material). These results clearly indicate the outstanding stability of the $\text{Ni}_x\text{P}/\text{NF}$ (DP) catalyst for the N_2H_4 electro-oxidation in alkaline condition.

3.3. Understanding the catalytic property of Ni_xP towards N_2H_4 electrooxidation

To rationalize such remarkably advanced catalyzing properties of the $\text{Ni}_x\text{P}/\text{NF}$ (DP) over the neat NF for the N_2H_4 electrooxidation, and to discern the activity boost upon phosphorization and especially identify the nature of active sites of the Ni_xP catalysts, we performed first-principles calculations to study the elementary steps ($\text{N}_2\text{H}_4 \rightarrow \text{N}_2\text{H}_3 \rightarrow \text{N}_2\text{H}_2 \rightarrow \text{N}_2\text{H} \rightarrow \text{N}_2$) involved in N_2H_4 electrooxidation on the f.c.c. Ni

(111) and hexagonal Ni_2P (001) surfaces [41]. The (111) plane is well known as the most stable Ni surface and the select of Ni_2P (001) surface as a model substrate was based on the experimental observations that the Ni_2P phase with a predominant (001) orientation exclusively distributed on the Ni_{12}P_5 surface, which made it readily accessible to the N_2H_4 reactant. Fig. 4 presents the Gibbs free energy diagram for the stepwise N_2H_4 dehydrogenation process with optimized structures on the two modelled surfaces. On both surfaces, only the H extraction from N_2H_2 is endothermic and all the other steps are exothermic in nature. A comparison of the calculated Gibbs free energy profiles suggested that the path of N_2H_4 dehydrogenation over Ni_2P (001) surface is energetically smoother than that on Ni (111). In particular, the rate-limiting transformation of N_2H_2 to N_2H on Ni_2P (001) was less endothermic by nearly 30% than that on Ni (111). These results clearly suggest that Ni_2P possesses a higher intrinsic activity than metallic Ni towards N_2H_4 electrooxidation. Our calculations further showed that, due to the formation of single-atom-like isolated Ni active sites by the surrounding P atoms (Fig. S8, Supplementary material), the Ni_2P (001)

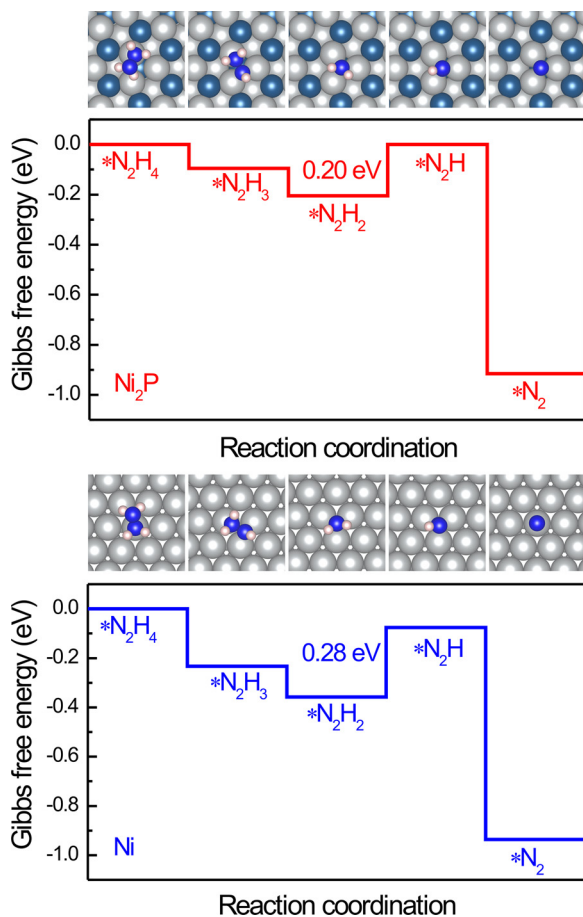


Fig. 4. The Gibbs free energy profiles for the stepwise N_2H_4 dehydrogenation process with optimized structures on Ni_2P (001) and Ni (111) surfaces. Grey, indigo, blue and white balls represent Ni, P, N and H atoms, respectively (for interpretation of the references to colour in this figure legend, the reader is referred to the web version of this article).

surface per unit provides a larger number of active sites than Ni (111) surface. Specifically, a (1×1) Ni_2P (001) surface ensures a comparable adsorption strength of N_2H_4 molecule (around -0.80 eV) to a (3×3) Ni (111) surface. But the area of the (1×1) Ni_2P (001) surface is just around 60% of the (3×3) Ni (111). Based on these calculation results, the experimentally observed superior electrocatalytic activity of Ni_xP nanowires array towards N_2H_4 electrooxidation should stem from a favorable combination of high intrinsic activity and high density of active sites of the Ni_2P surface, as well as the intrinsically high electrical conductivity of Ni_{12}P_5 and Ni_2P phases.

4. Conclusions

A supported nickel phosphides nanowire catalyst on Ni foam was synthesized by direct phosphorization method. The in situ grown nanowire arrays are composed of Ni_{12}P_5 and Ni_2P phases with Ni_2P nanoparticles exclusively distributing on the surface of Ni_{12}P_5 . Thus-prepared $\text{Ni}_x\text{P}/\text{NF}$ catalyst exhibits exceptionally high activity, excellent durability and nearly 100% selectivity towards the complete electro-oxidation of hydrazine, and the overall catalytic performance was comparable to the top-notch hydrazine electrooxidation catalysts reported to date. According to our first-principles calculations, the outstanding electrocatalytic performance should be primarily ascribed to the high intrinsic activity and high density of active sites of Ni_2P , as well as the good electrical conductivity of Ni_{12}P_5 and Ni_2P phases. Our experimental and theoretical results may provide insights and guidelines for future exploitation of high-performance phosphide-based

electrocatalysts for the applications of direct hydrazine fuel cell.

Acknowledgements

The financial supports for this research from the National Natural Science Foundation of China (Grant Nos. 51471168, 51671087 and 11504303), the Foundation for Innovative Research Groups of the National Natural Science Foundation of China (Grant No. 51621001), the Foundation for Research Groups of the Natural Science Foundation of Guangdong Province (Grant No. 2016A030312011) and the Special Support Plan for National 10000-talents Program are gratefully acknowledged.

Appendix A. Supplementary data

Supplementary material related to this article can be found, in the online version, at doi:<https://doi.org/10.1016/j.apcatb.2018.09.043>.

References

- [1] G.E. Evans, K.V. Kordes, *Science* 158 (1967) 1148–1152.
- [2] B.C. Steele, A. Heinzel, *Nature* 414 (2001) 345–352.
- [3] A. Serov, C. Kwak, *Appl. Catal. B-Environ.* 98 (2010) 1–9.
- [4] J. Seweryn, A. Lewera, *Appl. Catal. B-Environ.* 144 (2014) 129–134.
- [5] S. Kim, E.P. Ji, W. Hwang, Y.H. Cho, Y.E. Sung, *Appl. Catal. B-Environ.* 209 (2017) 91–97.
- [6] J.S. Guo, R.R. Chen, F.C. Zhu, S.G. Sun, H.M. Villullas, *Appl. Catal. B-Environ.* 224 (2018) 602–611.
- [7] A. Serov, M. Padilla, A.J. Roy, P. Atanassov, T. Sakamoto, K. Asazawa, H. Tanaka, *Angew. Chem. Int. Ed.* 53 (2014) 10336–10339.
- [8] J.R. Varcoe, P. Atanassov, D.R. Dekel, A.M. Herrling, M.A. Hickner, P.A. Kohl, A.R. Kucernak, W.E. Mustain, K. Nijmeijer, K. Scott, T. Xu, L. Zhuang, *Energy Environ. Sci.* 7 (2014) 3135–3191.
- [9] K. Asazawa, T. Sakamoto, S. Yamaguchi, K. Yamada, H. Fujikawa, H. Tanaka, K. Oguro, *J. Electroanal. Chem.* 516 (2009) B509–B512.
- [10] K. Asazawa, K. Yamada, H. Tanaka, A. Oka, M. Taniguchi, T. Kobayashi, *Angew. Chem. Int. Ed.* 46 (2007) 8024–8027.
- [11] D.A. Finkelstein, R. Imbeault, S. Garbarino, L. Roué, D. Guay, *J. Phys. Chem. C* 120 (2016) 4717–4738.
- [12] D.C.D. Oliveira, W.O. Silva, M. Chatenet, F.H.B. Lima, *Appl. Catal. B-Environ.* 201 (2017) 22–28.
- [13] L.Q. Ye, Z.P. Li, H.Y. Qin, J.K. Zhu, B.H. Liu, *J. Power Sources* 196 (2011) 956–961.
- [14] Q. Yi, W. Yu, *J. Electroanal. Chem.* 633 (2009) 159–164.
- [15] R. Crisafulli, V.V.S.D. Barros, F.E.R.D. Oliveira, T.D.A. Rocha, S. Zignani, L. Spadaro, A. Palella, J.A. Dias, J.J. Linares, *Appl. Catal. B-Environ.* 236 (2018) 36–44.
- [16] Y. Kuang, G. Feng, P.S. Li, Y. Bi, Y.M. Li, X.M. Sun, *Angew. Chem. Int. Ed.* 55 (2016) 693–697.
- [17] Y. Liang, Y. Zhou, J. Ma, J.Y. Zhao, Y. Chen, Y.W. Tang, T.H. Lu, *Appl. Catal. B-Environ.* 103 (2011) 388–396.
- [18] F. Yang, K. Cheng, G.L. Wang, D.X. Cao, *J. Electroanal. Chem.* 756 (2015) 186–192.
- [19] Z.Y. Lu, M. Sun, T.H. Xu, Y.J. Li, W.W. Xu, Z. Chang, Y. Ding, X.M. Sun, L. Jiang, *Adv. Mater.* 27 (2015) 2361–2366.
- [20] A.L. Cazetta, T. Zhang, T.L. Silva, V.C. Almeida, T. Asefa, *Appl. Catal. B-Environ.* 225 (2018) 30–39.
- [21] J.F. Huang, S.N. Zhao, W. Chen, Y. Zhou, X.L. Yang, Y.H. Zhu, C.Z. Li, *Nanoscale* 8 (2016) 5810–5814.
- [22] J. Sanabria-Chinchilla, K. Asazawa, T. Sakamoto, K. Yamada, H. Tanaka, P. Strasser, *J. Am. Chem. Soc.* 133 (2011) 5425–5431.
- [23] G. Feng, Y. Kuang, P.S. Li, N.N. Han, M. Sun, G.X. Zhang, X.M. Sun, *Adv. Sci.* 4 (2017) 1600179.
- [24] M. Sun, Z.Y. Lu, L. Luo, Z. Chang, X.M. Sun, *Nanoscale* 8 (2016) 1479–1484.
- [25] L. Zhou, M.F. Shao, C. Zhang, J.W. Zhao, S. He, D.M. Rao, M. Wei, D.G. Evans, X. Duan, *Adv. Mater.* 29 (2017) 1604080.
- [26] Z.W. Seh, J. Kibsgaard, C.F. Dickens, I. Chorkendorff, J.K. Nørskov, T.F. Jaramillo, *Science* 355 (2017) eaad4998.
- [27] C. Tang, R. Zhang, W.B. Lu, Z. Wang, D.N. Liu, S. Hao, G. Du, A.M. Asiri, X.P. Sun, *Angew. Chem. Int. Ed.* 56 (2017) 842–846.
- [28] G. Kresse, D. Joubert, *Phys. Rev. B* 59 (1999) 1758–1775.
- [29] J.P. Perdew, K. Burke, M. Ernzerhof, *Phys. Rev. Lett.* 77 (1996) 3865–3868.
- [30] M.K. Agusta, M. David, H. Nakanishi, H. Kasai, *Surf. Sci.* 604 (2010) 245–251.
- [31] M.K. Agusta, H. Kasai, *Surf. Sci.* 606 (2012) 766–771.
- [32] Y.B. He, J.F. Jia, H.S. Wu, *Appl. Surf. Sci.* 339 (2015) 36–45.
- [33] P. Liu, J.A. Rodriguez, T. Asakura, J. Gomes, K. Nakamura, *J. Phys. Chem. B* 109 (2005) 4575–4583.
- [34] G. Kresse, J. Furthmüller, *Comput. Mater. Sci.* 6 (1996) 15–50.
- [35] Y. Zhang, X. Chen, Y. Huang, C. Zhang, F. Li, H. Shu, *J. Phys. Chem. C* 121 (2017) 1530–1536.
- [36] M. Ledendecker, S.K. Calderyn, C. Papp, H.P. Steinrük, M. Antonietti, M. Shalom, *Angew. Chem. Int. Ed.* 54 (2015) 12361–12365.

- [37] X.G. Wang, Y.V. Kolen'ko, X.Q. Bao, K. Kovnir, L.F. Liu, *Angew. Chem. Int. Ed.* 54 (2015) 8188–8192.
- [38] Z.Z. Ma, R.X. Li, M. Wang, H.J. Meng, F. Zhang, X.Q. Bao, B. Tang, X.G. Wang, *Electrochim. Acta* 219 (2016) 194–203.
- [39] C.C. Hou, Q.Q. Chen, C.J. Wang, F. Liang, Z.S. Lin, W.F. Fu, Y. Chen, *ACS Appl. Mater. Interfaces* 8 (2016) 23037–23048.
- [40] J. Xiao, Q.Y. Lv, Y. Zhang, Z.Y. Zhang, S. Wang, *RSC Adv.* 6 (2016) 107859–107864.
- [41] G. Kresse, J. Furthmüller, *Phys. Rev. B* 54 (1996) 11169–11186.